

1 **Acoustically Manipulating Internal Structure of Disk-in-Sphere Endoskeletal Droplets**

2 Gazendra Shakya^{#1}, Tao Yang^{#1}, Yu Gao¹, Apresio K. Fajrial¹, Baowen Li¹, Massimo Ruzzene¹, Mark

3 A. Borden^{1,2}, Xiaoyun Ding^{1,2*}

4 ¹Paul M. Rady Department of Mechanical Engineering, University of Colorado, Boulder, CO 80309,

5 USA

6 ²Biomedical Engineering Program, University of Colorado, Boulder, CO 80309, USA

7 *Corresponding Author

8

9 Abstract

10 Manipulation of micro/nano particles has been well studied and demonstrated by optical, electromagnetic,
11 and acoustic approaches, or their combinations. Manipulation of internal structure of droplet/particle is
12 rarely explored and remains challenging due to its complicated nature. Here we demonstrated the
13 manipulation of internal structure of disk-in-sphere endoskeletal droplets using acoustic wave for the first
14 time. We developed a model to investigate the physical mechanisms behind this novel phenomenon.
15 Theoretical analysis of the acoustic interactions indicated that these assembly dynamics arise from a
16 balance of the primary and secondary radiation forces. Additionally, the disk orientation was found to
17 change with acoustic driving frequency, which allowed on-demand, reversible adjusting disk orientations
18 with respect to the substrate. This novel dynamic behavior leads to unique reversible arrangements of the
19 endoskeletal droplets and their internal architecture, which may provide a new avenue for directed
20 assembly of novel hierarchical colloidal architectures and intracellular organelles or intra-organoid
21 structures.

22

23 Introduction

24 Manipulating particles from nanometer scale to micrometer and millimeter scale, such as molecules,
25 cells, colloids, droplets, and small model organisms, has been important in biology, chemistry, and
26 medicine. Micro manipulation can be achieved by optical, electromagnetic, mechanical, acoustic
27 approaches or their combinations. For instance, optical and nanorobotic methods have been successfully
28 used for manipulation in nano and micro scale¹⁻³. Electrical and acoustic methods have achieved high
29 throughput particle manipulation for applications such as bioparticle patterning, protein characterization,
30 cell separation and droplet sorting, etc⁴⁻⁶. However, an advanced manipulation of internal structure of
31 complex colloids has been long-standing challenging and rarely reported so far.

32 Endoskeletal droplets are a novel class of complex colloids containing a solid internal phase cast
33 within a liquid emulsion droplet. In an early example, petrolatum-in-hexadecane droplets were shown to

34 have controllable shape by microfluidic processing and manipulation of the balance between internal
35 elasticity and surface tension⁷. Such droplets have been used to form novel fluid networks⁸, which change
36 their orientation and shape in response to external stimuli^{9,10}. Recently, solid hydrocarbon in liquid
37 fluorocarbon were described, in which melting of the internal solid hydrocarbon phase triggered
38 vaporization of the fluorocarbon liquid phase¹¹. Additionally, solid-in-liquid perfluorocarbon droplets
39 were made that exhibited a unique droplet structure: a fluorocarbon solid disk suspended inside a liquid
40 fluorocarbon droplet¹¹.

41 Here, we describe the synthesis of monodisperse disk-in-sphere perfluorocarbon droplets and their
42 internal structure manipulation for the first time in an acoustic field. Among the host of attractive and
43 repulsive interactions available to colloidal particles¹²⁻¹⁵, acoustic radiation forces, induced by acoustic
44 fields, have proved to be an efficient way to manipulate particles. Even though the particle responses to
45 acoustic radiation forces have been used for applications such as particle separation¹⁶⁻¹⁹, particle
46 manipulation^{20,21} and assembly of complex structures^{22,23}, the manipulation of internal structures within
47 endoskeletal colloids has not yet been reported. In this work, two unprecedented phenomena were
48 discovered. First, we observed that the droplets clustered in such a way that the disks oriented
49 orthogonally to the cluster centroid. Second, we found that the disk orientation could be manipulated by
50 changing the frequency of the acoustic waves. These novel behaviors can be described by an investigation
51 of their acoustic interactions and a balance of the primary and secondary radiation forces, and they offer
52 the tantalizing possibility of acoustically constructed colloidal assemblies with dynamic and tunable
53 internal structures.

54 Results and Discussion

55 Microfluidic fabrication of endoskeletal droplets

56 Disk-in-sphere endoskeletal droplets consisting of solid perfluorododecane (PFDD, C₁₂F₂₆, $\rho_s=1.73$
57 g/cm³, $c_s=641$ m/s²²) and liquid perfluorohexane (PFH, C₆F₁₄, density $\rho_l=1.69$ g/cm³ and sound velocity

58 $c_l = 479 \text{ m/s}^{24}$) were fabricated using a flow focusing microfluidic channel (Fig. 1A, B, C). Detailed
59 information about the device fabrication and droplet fabrication can be found in the methods section. The
60 device was selectively heated to melt the solid component (45 mol%) prior to droplet generation. Thus,
61 initially isotropic liquid droplets of uniform size (radius $a = 4.78 \pm 0.25 \text{ }\mu\text{m}$) (Supplementary Fig. 1A)
62 were produced that contain a mixture of the solid and liquid fluorocarbons (FC) (Fig. 1D) in a liquid state
63 at $\sim 42 \text{ }^\circ\text{C}$. When cooled, the PFDD solidified to create the unique disk-shaped structure (radius $R = 3.35$
64 μm , thickness $h = 2.4 \text{ }\mu\text{m}$) inside each individual droplet (Fig. 1E). Although the disks were confined
65 inside the liquid PFH droplets, they were observed to rotate and translate within the confinements of the
66 droplet (Supplementary Fig. 1B). The orientation is denoted as ‘parallel’ and ‘perpendicular’ with respect
67 to the substrate. In the parallel orientation the disks appeared as circles, as shown by the black arrows in
68 Fig. 1E, while in the perpendicular orientation the disks appeared as rectangles as highlighted by the red
69 arrows.

70 Acoustically driven endoskeletal droplet patterning

71 We incorporated two counter-propagating surface acoustic waves (SAWs) with center frequency of 20
72 MHz, generated by applying voltage to interdigital transducers (IDTs) deposited on a piezoelectric
73 material (Lithium niobate, LiNbO_3) (Fig. 2A). These SAWs traveled through an aqueous phase, where
74 the droplets were suspended, confined in a polydimethylsiloxane (PDMS) channel (2 mm width, 18 μm
75 height) attached to a Lithium niobate substrate. The counter-propagating acoustic waves formed one-
76 dimensional (1D) standing surface acoustic wave (standing SAW) in the x-direction within the channel
77 (Fig. 2A).

78 We observed the endoskeletal droplets suspended in this standing SAW field. The droplets attracted
79 one another and moved to form clusters of various sizes (Supplementary Movie 1). Fig. 2B-G shows an
80 example of these clusters arranged under the standing SAW. For single droplets (monomers), the disk was
81 found to be parallel to the substrate and pushed up to the top of the droplet (Fig. 2C, Supplementary
82 Movie 2). For 2-droplet clusters (dimers), the orientation of the disk was midway ($\sim 45^\circ$) between the

83 parallel and the perpendicular orientations (Fig. 2D, Supplementary Movie 3). For clusters containing
84 more than 2 droplets, the disks were oriented perpendicular to the substrate (Fig. 2E-G, Supplementary
85 Fig. 2). Interestingly, for these larger clusters, the disks always arranged such that the normal of the basal
86 plane of each disk pointed to the centroid of the cluster (Supplementary Fig. 2).

87 Furthermore, the solid disk inside a droplet only rearranged when it came close to another particle.
88 This can be seen in Supplementary Movie 1, where the disks begin rearranging as the droplets come into
89 close proximity of each other. This neighbor-dependent behavior suggested an interaction force between
90 the approaching particles. To better understand this behavior, we turned to droplets without internal
91 structures.

92 Acoustic assembly of liquid only fluorocarbon (FC) droplets

93 Liquid-only PFH droplets of similar size ($\sim 5 \mu\text{m}$ radius) as the endoskeletal droplets were generated
94 using the same microfluidic and suspended in the same SAW setups (Fig. 2A). The liquid-only PFH
95 droplets were observed to cluster in a similar manner as the endoskeletal PFDD-in-PFH droplets (Fig.
96 2H-J). Samples containing a mixture of PFH and endoskeletal droplets were also observed to cluster in a
97 similar manner (Fig. 2K-M). This behavior indicated that the disks themselves did not cause the droplets
98 to cluster. Moreover, the disks arranged in similar orientations, regardless of whether the neighboring
99 droplet contained a disk (Fig. 2E-M). This result indicated that the disk rotation and orientation was not
100 caused by neighboring disks.

101 Theoretical investigation of clustering behavior

102 Acoustic radiation forces are responsible for particle motion in an acoustic field. The primary radiation
103 potential experienced by the droplets due to acoustic pressure gradients in the limit of $a \ll \lambda_w$ (where λ_w
104 is the acoustic wavelength in water and is $\sim 74 \mu\text{m}$ for 20 MHz), also called Gor'kov potential²⁵, is given
105 by^{26,27}:

106

$$U_{rad} = V_p \left(\frac{1}{2} f_{0,l/w} \beta_w \langle p_1^2 \rangle - \frac{3}{4} f_{1,l/w} \rho_w \langle v_1^2 \rangle \right) \quad (1)$$

$$\text{Here, } f_{0,l/w} = 1 - \frac{\beta_l}{\beta_w} \text{ and } f_{1,l/w} = \frac{2(\rho_l - \rho_w)}{2\rho_l + \rho_w} \quad (2a) \text{ \& } (2b)$$

107

108 where V_p is the droplet volume, $f_{0,l/w}$ and $f_{1,l/w}$ are the monopole and dipole scattering factors (l/w for

109 PFH liquid/water system), $\beta = \frac{1}{\rho c^2}$ is the compressibility, ρ is the density, c is the speed of sound,

110 subscript l signifies PFH liquid and subscript w signifies water, p_1 is the first order pressure amplitude, v_1

111 is the particle velocity and $\langle \dots \rangle$ stands for the time average. For a 1D standing acoustic wave, i.e.,

112 incoming acoustic pressure $p_{in} = p_0 \cos(k_w x)$ (where p_0 is the pressure amplitude and $k_w = \frac{2\pi}{\lambda_w}$ is the

113 wavenumber in water), the primary radiation force F_{pri} can be simplified as^{26,27}:

114

$$\mathbf{F}_{pri} = -\nabla U_{rad} = \frac{1}{2} V_p E_0 \Phi_{l/w} k_w \sin(2k_w x) \hat{\mathbf{x}} \quad (3)$$

115

116 where $E_0 = \frac{1}{2} \beta_w p_0^2$ is the acoustic energy density and $\Phi_{l/w} = f_{0,l/w} + \frac{3}{2} f_{1,l/w}$ is the acoustic contrast

117 factor²⁶⁻²⁹. The sign of the acoustic contrast factor determines the direction of the primary radiation force

118 (towards pressure node or antinode) that a particle experiences at its location within the standing SAW

119 field. For our droplet emulsion (PFH liquid in water), Φ is negative (-4.26), hence the PFH droplets were

120 driven to the pressure antinodes (Fig. 3A).

121 When one droplet approaches another as they migrate to the antinode, the acoustic wave scattering

122 from the neighboring body induces an additional interaction force, called the secondary radiation force²⁸.

123 The interaction energy at the anti-nodal line between two particles with negative contrast factor (two PFH

124 droplets in this case) in the anti-nodal plane under a 1D standing wave was simplified²⁸ as:

125

$$\mathbf{U}_{sec} = \frac{V_p^2 E_0 k_w^2}{8\pi r} (3 \cos^2 \delta f_{0,l/w} f_{1,l/w} - 2 f_{0,l/w}^2) \quad (4)$$

126

127 where r is the distance between two droplet centers and δ is the orientation angle between two droplets
128 (Fig. 3B) with respect to the wave propagation direction (x -axis). The secondary radiation force ($\mathbf{F}_{sec} =$
129 $-\nabla U_{sec}$) derived from Eq. 4 is consistent with the well-known Bjerknes forces for gas bubbles in short-
130 range³⁰. The calculated secondary interaction energy from Eqn. 4 between two contacting PFH droplets
131 (i.e., $r = 2a$) is shown in Fig. 3B (blue). Since the magnitude of $f_{0,l/w} = 4.74$ is about one order larger than
132 $f_{1,l/w} = 0.32$, the monopole effect dominates and the interactions between two spheres are almost
133 isotropic attractions (Supplementary Fig. 3A). As a result, two-dimensional closed packed clusters are
134 formed (Fig. 2H-J, 3C). This type of clustering behavior is usually observed in polystyrene (PS)
135 spheres³¹, cells^{31,32} and silicone microspheres¹⁴ under two-dimensional (2D) standing waves where
136 acoustic waves propagate in both the x and y directions. For comparison, the interaction energy of two
137 contacting polystyrene (PS) particles ($f_{0,s/w} = 0.46$, $f_{1,s/w} = 0.038$, and $\Phi_{s/w} = 0.517$) with the same size
138 placed at the nodal plane (Eqn. S3) of a 1D standing SAW was also plotted in Fig. 3B (red). For PS
139 particles, dipolar interactions with preferential angle parallel to the nodal lines are expected
140 (Supplementary Fig. 3B), which explains why colloidal chains of PS particles were formed on our
141 standing SAW device (Fig. 3D), and as seen in similar studies done on PS particles by Shi et al.³¹ and
142 Vakarelski et al³³.

143 Interpreting disk arrangement behavior

144 From the previous discussions, we can conclude that the aggregation of endoskeletal droplets as well
145 as liquid PFH droplets were due to the combined effects of primary and secondary radiation forces. To
146 better understand the unique orientations of the solid disks inside the endoskeletal droplets, we performed
147 finite element simulations using COMSOL (version 5.0) where the forces and torques on the inner disk
148 were calculated following prior work^{26,34,35} (see Supplementary Section 2). The equilibrium disk
149 orientation was determined by the zero-torque configuration and is shown in Fig. 4A, B. Here, the angle
150 θ_i is defined as the angle between the disk (of i^{th} droplet) and the nodal line (positive y -axis), whereas the

151 angle α is defined as the angle between the nodal line and the line joining the centroid and the center of
 152 the 1st droplet (which determines the orientation of the whole cluster). The equilibrium angles of the
 153 disks are given by θ_i values at zero torque. These calculated equilibrium angles (Fig. 4B) are consistent
 154 with the orientations of disks seen in experiments (Fig 2E). These equilibrium angles were also calculated
 155 at different cluster orientation angles (α), which is shown in Supplementary Fig. 5 along with the
 156 experimentally observed θ values. Similar equilibrium angles at zero torque configurations were
 157 calculated for different droplet clusters (Supplementary Table 1), which match the experimental
 158 observations as well.

159 Note that the results shown in Fig. 4A and 4B assume the disks to be at the droplet centers and not
 160 translating (only rotating). In reality, as the inner PFDD solid has a positive acoustic contrast factor
 161 against surrounding PFH liquid ($f_{0,s/l} = 0.45$, $f_{1,s/l} = 0.016$, and $\Phi_{AC,s/w} = 0.48$), disks are expected to be
 162 pushed to the edges of the droplets where local pressure minima exist (Fig. 2D-G, Supplementary Fig. 2,
 163 Supplementary Movie 1). However, translation did not affect the equilibrium disk orientation angles. This
 164 was shown by performing disk dynamics simulations that show behavior similar to what was seen in
 165 experiments, where the disks were pushed to the far edges of the droplets but retained their equilibrium
 166 angles (Supplementary Movie 4 and see Supplementary Section 3).

167 Once the equilibrium disk position and orientation were determined from the dynamic simulation, the
 168 local Gor'kov potential (U_{rad}/V_p) density and radiation force density (F_{pri}/V_p) on the disks inside
 169 droplets of a cluster were calculated, and is shown in Fig. 4C-I. The local forces pointing from the droplet
 170 center to the edge explains the origin of disk movement and final positions for multi-droplet clusters.

171 However, the differences in disk alignment seen in monomers and dimers suggest additional wave
 172 contributions. Due to the wave velocity differences in water and the solid substrate, the surface wave
 173 generated from the IDT's traveled into the water (i.e., "leaky" waves) at the Rayleigh angle $\theta_R =$
 174 $\text{acos}\left(\frac{k_{LN}}{k_w}\right)$, where $k_{LN} = \frac{2\pi}{\lambda_{LN}}$ is the wavenumber in the solid lithium niobate substrate (Fig 4J). Thus,
 175 these two counter-propagating leaky waves formed a quasi-standing wave in the z-axis along with

176 forming a standing wave in the x-axis (Fig. 4J) (Supplementary Section 4). As a result, a more realistic
 177 pressure distribution can be approximated as: $p_{in}' = p_0 \cos(k_{LN}x) \cos(k_w \sin \theta_R z)$ ³⁶. This pressure
 178 amplitude distribution was also confirmed with numerical simulation results (Supplementary Fig. 8),
 179 taking the leaky wave component into consideration following Nama et al.³⁷, Devandran et al.³⁸ and
 180 Barnkob et. al.³⁹. The additional standing wave component in the z-axis generated additional torque,
 181 which aligned the inner disks parallel to the xy plane, as in a single droplet. When simplified as a Raleigh
 182 disk ($R \ll \lambda_w$)⁴⁰, the torque on the disk in x-axis was shown as⁴¹:

$$\tau_x = -\frac{4}{3} \rho_l R^3 v_{rms}^2 \sin(2\varphi) \quad (5)$$

183 where v_{rms} is the root-mean-square of particle velocity v_1 and the angle φ is the angle between v_1 and
 184 the orientation of the disk (Fig. 4K). As a result, the equilibrium disk orientation was along the particle
 185 velocity direction, i.e., $\varphi=0$. The particle velocity v_1 is the sum of contributions from the primary
 186 radiation v_{pri} and secondary radiation v_{sec} vectors, i.e., $\mathbf{v}_1 = \mathbf{v}_{pri} + \mathbf{v}_{sec}$. The particle velocity from
 187 primary radiation on each disk was the same, as shown by $\mathbf{v}_{pri} \sim \frac{p_0}{\rho_l c_l} k_w \sin \theta_R a \hat{\mathbf{z}}$ (see Supplementary
 188 Section 4).

189 For a monomer where there is no secondary radiation force contribution from a neighboring droplet,
 190 the effect of the leaky wave was observed in the disks, which rose to the top and oriented parallel to the
 191 substrate. This was shown both in experiments (Fig. 2C, Supplementary Movie 2) as well as dynamic
 192 simulations (Fig. 4C, Supplementary Movie 5). In case of the dimer, the disk orientation was balanced by
 193 the primary radiation torque turning the disk parallel to the substrate and the secondary radiation torque
 194 aligning the disk perpendicular to the substrate. The particle velocity from secondary radiation is shown
 195 along the interparticle direction as: $\mathbf{v}_{sec} = -\frac{f_{0,l/w}}{3} \frac{p_0}{\rho_l c_l} k_l a \hat{\mathbf{r}}$. As the two particle velocities are of similar
 196 magnitude, the equilibrium disk orientation is $\sim 45^\circ$ (135°) with the z-axis, consistent with the
 197 experimental results (Fig. 2D, Supplementary Movie 3) and dynamic simulation results (Fig. 4D,
 198 Supplementary Movie 6). With more droplets joining to form a bigger cluster, the particle velocity from

199 secondary radiation was enhanced with all pairwise scattering from neighboring droplets (see
200 Supplementary Section 4 for quantitative scaling of secondary radiation particle velocity for a trimer).
201 Thus, the equilibrium disk orientation favored perpendicular alignment due to the dominating secondary
202 effects, which is consistent with experimental observations (Fig. 2E) as well as numerical dynamic
203 simulation (Fig. 4E, Supplementary Movie 4). This can be seen in clusters of 3 or more droplets, where
204 all of them showed similar perpendicular orientation of the disks (Fig 2E-G).

205 External control over the disk orientation

206 From the equations for the primary and secondary radiation forces (Eq. 3 and Eq. 4), we realized that
207 the primary radiation force is proportional to the wavenumber (proportional to frequency), whereas the
208 secondary radiation force is proportional to the wavenumber raised to the power of 2. This implies that
209 the secondary radiation force is more sensitive to the frequency of the wave than the primary radiation
210 force. Also, from our discussion in the previous section, we can summarize that the primary radiation
211 force is acting to push and rotate the disks to the top in a parallel position (parallel to substrate), whereas
212 the secondary radiation force is acting to flip the disk to the perpendicular position (perpendicular
213 substrate). Using the same logic, we tried manipulating the frequency of our acoustic wave in order to
214 externally manipulate the orientation of the disks inside the droplets. For this purpose, a chirped IDT
215 device (IDT device that can generate SAW in different frequencies) was fabricated that could generate
216 SAW at both 10 and 20 MHz frequencies²⁰.

217 At a frequency of 10 MHz, due to the smaller secondary radiation force compared to the primary
218 radiation force, the disks in all the clusters oriented parallel to the substrate (Fig. 5A, Supplementary
219 Movie 7) compared to the disks being perpendicular at 20 MHz (Supplementary Movie 1). To analyze
220 this effect of frequency, numerical simulations were performed on dimers and trimers at a frequency of 10
221 MHz. For dimers, the simulation results show that the equilibrium orientation angle for the disks was $\sim 23^\circ$
222 with the z-axis, which is much lower than the orientation angle at a frequency of 20 MHz (45°) (Fig. 5B
223 vs. 4D, Supplementary Movie 3, Supplementary Movie 6). The effect of the difference in frequency on

224 orientation behavior was clearly seen in 3-droplet clusters (Fig. 5A (ii), Supplementary Movie 8). To
225 demonstrate the utility of this behavior, we repeatedly switched the frequencies from 20 to 10 MHz and
226 vice versa and found tunable orientation of the disks from perpendicular (at 20 MHz) to parallel (at 10
227 MHz) and vice versa (Fig. 5C, Supplementary Fig. 10, Supplementary Movie 9). For better visualization
228 of this phenomenon, we incorporated cross-polarized microscopy (CPM)⁴² technique to image the disks.
229 Under CPM, due to the difference in the crystal orientation of the solid, the disk was only visible when
230 the disks were oriented in the long axis (perpendicular to the substrate). Hence, at the frequency of 10
231 MHz (when disks were parallel), the field is dark, whereas when the frequency was changed to 20 MHz,
232 the disks brighten up (Fig. 5C, Supplementary Movies 10 and 11). This on-demand reorientation of the
233 disks could in principle be used for applications involving acoustic-optical filters, as the total light
234 intensity can be accurately switched from high to low as shown in Fig. 5D. This behavior was
235 reproducible and was observed for droplets within larger cluster sizes as well (Supplementary Fig. 10,
236 Supplementary Movie 11).

237 In summary, we demonstrated a unique acoustic manipulation of internal structure of disk-in-sphere
238 endoskeleton droplets, a very interesting yet challenging manipulation that has not yet been reported.
239 Under a one-dimensional standing acoustic wave, endoskeletal droplets move to the antinode and attract
240 each other to form clusters. However, a repulsive secondary radiation force between the disks and drops
241 caused the disks to align perpendicularly to the substrate and perpendicularly to the droplet cluster
242 centroid. This orientation of the internal disks could be reversibly manipulated by simply using different
243 frequencies of acoustic wave, which changes the balance between the primary and secondary radiation
244 forces responsible for the disk orientation. This distinctive dynamic manipulation could potentially
245 provide further opportunities for directed colloidal assembly with dynamic and acoustically tunable
246 internal structures and pave the way towards manipulation of the internal structures of organoids and
247 cells.

248 Materials and Methods

249 **Materials.** The following chemicals were used as received: perfluorohexane (PFH) (C_6F_{14} , 99%,
250 FluoroMed, Round Rock, TX, USA); perfluorododecane (PFDD) ($C_{12}F_{26}$, >99%, Fluoryx Labs, Carson
251 City, NV, USA); 1,2-dibehenoyl-sn-glycero-3-phosphocholine (DBPC) (99%, Avanti Polar Lipids,
252 Alabaster, AL, USA); N-(methylpolyoxyethyleneoxycarbonyl)-1,2-distearoyl-sn-glycero-3-
253 phosphoethanolamine (DSPE-PEG5K) (NOF America, White Plains, NY, USA); polydimethylsiloxane
254 (PDMS) (Sylgard 184 Silicone Elastomer, Dow, Midland, MI; positive photoresist (MEGAPOSIT
255 SPR220-3.0, Dupont, Wilmington, DE); Trichloro(1H,1H,2H,2H-perfluorooctyl)silane, Polyvinyl
256 Alcohol (PVA) (Sigma Aldrich, St. Louis, MO); photoresist developer ((MEGAPOSIT MF-26A, Dupont,
257 Wilmington, DE; ultrapure deionized (DI) water from Millipore Direct-Q (Millipore Sigma, St. Louis,
258 MO, USA).

259 **Preparation of the surfactant (lipid) solution.** The lipid solution was formulated by suspending DBPC
260 and DSPE-PEG5K (9:1 molar ratio) at a total lipid concentration of 10 mg/mL in DI water. The lipids
261 were first dissolved and mixed in chloroform in a glass vial, and then the solvent was removed to yield a
262 dry lipid film at 35 °C and under vacuum overnight. The dry lipid film was rehydrated using DI water and
263 then sonicated at 75 °C at low power (3/10) for 10 min to convert the multilamellar vesicles to
264 unilamellar liposomes.

265 **Fabrication of flow focusing PDMS device.** Standard soft lithography techniques were used to construct
266 the polydimethylsiloxane (PDMS) devices. Two device designs were prepared for the PDMS devices.
267 One for the droplet generation and another one for SAW experiments. For both, masks for lithography
268 were drawn using CleWin4 layout editor software (WeiWeb, Hengelo, The Netherlands) (Fig. 1A) and
269 transparency masks were printed commercially (CAD/Art Services, Bandon, OR) at high resolution. To
270 create the silicon mold, a layer of positive photoresist (MEGAPOSIT SPR220-3.0, Dupont, Wilmington,
271 DE) was spin-coated on a silicon wafer (El-Cat Inc., Ridgefield Park, NK), pattern-transferred with a
272 mask exposer (MJB4, KARL SUSS, Germany), and developed in a photoresist developer (MEGAPOSIT

273 MF-26A, Dupont, Wilmington, DE). Afterwards, the substrate was dry-etched with SF₆ plasma
274 (PlasmaSTAR, AXIC Inc., Santa Clara, CA). The silicon mold was silanized by vapor deposition of
275 Trichloro(1H,1H,2H,2H-perfluorooctyl)silane into the mold before use. PDMS pre-polymers (Sylgard
276 184 Silicone Elastomer, Dow, Midland, MI) were mixed (10:1 weight ratio of base:curing agent),
277 degassed in a vacuum desiccator for 30 mins, cast into the silanized silicon mold and cured at 65°C
278 overnight. After curing, individual PDMS devices were cut to shape from the mold.

279 Final device (for droplet generation) was prepared by treating the glass slide and the precut PDMS
280 device with air plasma using plasma wand (BD-10AS High Frequency Generator, Electro Technic
281 Products, Chicago, IL) for 30 seconds. The two surfaces were brought into contact for proper bonding.
282 1% PVA solution was put and left in the channels for 15 mins to make them hydrophilic⁴³. The excess
283 PVA solution was flushed out and the device was heated at 115 °C for 15 mins to vaporize any excess
284 water in the channels. Devices were then heated at 65 °C overnight.

285 **Fabrication of interdigital transducers (IDTs).** 128° Y-X cut Lithium Niobate, LiNbO₃, wafers were
286 purchased (Precision Micro-Optics, Burlington, MA) and cleaned by sonicating in acetone, isopropyl
287 alcohol and deionized (DI) water for 5 minutes each. The interdigitated electrodes (IDTs) were patterned
288 by standard microfabrication techniques. Typically, the LiNbO₃ was spin-coated with positive photoresist
289 (S1813, thickness of ~1.5 μm), and exposed to UV light under a mask. The exposed photoresist was
290 dissolved in MF-26A Developer. The IDTs were finally formed by E-beam evaporation (10 nm Cr, 100
291 nm Au) and lift-off processes. Furthermore, 300 nm of SiO₂ was deposited on the substrate by magnetron
292 sputtering to prevent corrosion of the IDTs and to enhance channel bonding. The IDTs consist of 20
293 finger-pairs with a 10 mm aperture and a 200 μm periodicity (50 μm finger width), and the resonance
294 frequency was then measured using a Keysight E5061B vector network analyzer (VNA) at 19.8 MHz.

295 **Synthesis of endoskeletal droplets.** The solid (perfluorododecane, C₁₂F₂₆) and the liquid
296 (perfluorohexane, C₆F₁₄) were mixed at a ratio of 45 mole percent solid. The mixture was heated until the
297 solids melted (~ 45 °C) in a heated water bath while intermittently stirring the mixture in a vial mixer
298 (Mini Vortexer, Fisher Scientific). The liquid mixture was put in a glass syringe (Gastight 1750,

299 Hamilton, Reno, NV) that was continuously heated using a syringe heater (Syringe Heater, New Era
300 Pump Systems, Farmingdale, NY) set at 50 °C to keep the FC mixture in liquid phase. This syringe was
301 set in a syringe pump (Fusion 4000, Chemyx, Stafford, TX) and was connected to the FC inlet of the
302 PDMS device using flexible plastic tubing (OD 0.07 inches, ID 0.04 inches, Tygon) and steel tube (18 G,
303 204 SS, Component Supply, Sparta, TN). The tubes were heated using a heat lamp (BR40 Incandescent
304 Heat lamp, 125 W, GE) and focusing the heat on the tubes using curved aluminum foil. The PDMS
305 device itself was placed on top of a flexible heater (Kapton KHLV-102/10-P, Omega Engineering,
306 Norwalk, CT, USA) attached to a power supply (Agilent E3640A, Agilent Technologies, Santa Clara,
307 CA, USA) which continuously heated the PDMS device. The PDMS device setup was mounted on a
308 microscope (Olympus IX71, Olympus Life Sciences) and images/videos were recorded using a digital
309 CCD camera (Qimaging QIClick digital CCD camera). The syringe containing lipid solution was set in
310 another syringe pump (GenieTouch, Kent Scientific) and was connected to the lipid inlet of the PDMS
311 device using the same plastic tubing and steel tube. The lipid solution and FC mixture were injected at
312 flowrates of 20 $\mu\text{l}/\text{min}$ and 1 $\mu\text{l}/\text{min}$ respectively. The generated droplets were collected from the
313 collection chamber (outlet) into a 2 ml glass vial and the emulsion was cooled to solidify the endoskeleton
314 and stored in the fridge until used.

315 **Synthesis of liquid PFH droplets.** Liquid perfluorohexane (PFH, C_6F_{14}) droplets were generated using
316 the same PDMS microfluidic device (Fig. 1A-C). PFH was set in a syringe pump and connected to the FC
317 inlet. Lipid solution (similar to earlier section) was used as the aqueous phase. The lipid solution and FC
318 phase were injected at flowrates of 20 $\mu\text{l}/\text{min}$ and 1 $\mu\text{l}/\text{min}$ respectively.

319 **Surface acoustic wave directed assembly.** The PDMS channel was plasma treated before attaching it to
320 the LiNbO₃ device to treat the PDMS surface and make it hydrophilic. Endoskeletal droplet solution was
321 diluted (10X) and 10 μl of the diluted solution was pipetted at the edge of the PDMS device channel such
322 that the emulsion would flow into the device by capillary effect. When the channel was fully wetted, the
323 two ends were sealed using vacuum grease (Dow Corning, Houston, TX, USA). The IDTs were
324 connected to a RF Signal generator (SDG 5082, Silgent Technologies) and amplified by a power

325 amplifier (403LA Broadband Power Amplifier, Electronics, and Innovation). The IDT device with the
326 PDMS channel was mounted on an inverted microscope (Nikon Eclipse Ti2 Inverted Microscope,
327 Melville, NY, USA) fitted with Nikon Plan Flour 4X, 10X and 40X objectives. The microscope was
328 attached to a digital CMOS camera (Hamamatsu C11450 ORCA Flash-4.0LT, Bridgewater, NJ, USA).
329 Images were acquired using a custom-built LabVIEW VI.

330 **Cross polarized microscopy.** Images and videos were recorded by using two polarizer filters at 90° with
331 each other. One of the filters was placed before the sample and the other was placed after the sample in
332 the light path of the inverted microscope.

333 References

- 334 1. Yang, A. H. J. *et al.* Optical manipulation of nanoparticles and biomolecules in sub-wavelength slot
335 waveguides. *Nature* **457**, 71–75 (2009).
- 336 2. Lin, L. *et al.* Opto-thermoelectric nanotweezers. *Nature Photon* **12**, 195–201 (2018).
- 337 3. Zhang, Z., Wang, X., Liu, J., Dai, C. & Sun, Y. Robotic Micromanipulation: Fundamentals and
338 Applications. *Annu. Rev. Control Robot. Auton. Syst.* **2**, 181–203 (2019).
- 339 4. Yao, J., Zhu, G., Zhao, T. & Takei, M. Microfluidic device embedding electrodes for dielectrophoretic
340 manipulation of cells-A review. *ELECTROPHORESIS* **40**, 1166–1177 (2019).
- 341 5. Baudoin, M. & Thomas, J.-L. Acoustic Tweezers for Particle and Fluid Micromanipulation. *Annu. Rev.*
342 *Fluid Mech.* **52**, 205–234 (2020).
- 343 6. Kolesnik, K., Xu, M., Lee, P. V. S., Rajagopal, V. & Collins, D. J. Unconventional acoustic approaches
344 for localized and designed micromanipulation. *Lab Chip* **21**, 2837–2856 (2021).
- 345 7. Caggioni, M., Traini, D., Young, P. M. & Spicer, P. T. Microfluidic production of endoskeleton
346 droplets with controlled size and shape. *Powder Technology* **329**, 129–136 (2018).
- 347 8. Prileszky, T. A. & Furst, E. M. Fluid Networks Assembled from Endoskeletal Droplets. *Chem. Mater.*
348 **28**, 3734–3740 (2016).

- 349 9. Caggioni, M., Bayles, A. V., Lenis, J., Furst, E. M. & Spicer, P. T. Interfacial stability and shape change
350 of anisotropic endoskeleton droplets. *Soft Matter* **10**, 7647–7652 (2014).
- 351 10. Prileszky, T. A. & Furst, E. M. Magnetite nanoparticles program the assembly, response, and
352 reconfiguration of structured emulsions. *Soft Matter* **15**, 1529–1538 (2019).
- 353 11. Shakya, G. *et al.* Vaporizable endoskeletal droplets via tunable interfacial melting transitions. *Sci Adv*
354 **6**, eaaz7188 (2020).
- 355 12. Erb, R. M., Son, H. S., Samanta, B., Rotello, V. M. & Yellen, B. B. Magnetic assembly of colloidal
356 superstructures with multipole symmetry. *Nature* **457**, 999–1002 (2009).
- 357 13. Liu, M., Zheng, X., Grebe, V., Pine, D. J. & Weck, M. Tunable assembly of hybrid colloids induced by
358 regioselective depletion. *Nature Materials* **19**, 1354–1361 (2020).
- 359 14. Owens, C. E., Shields, C. W., Cruz, D. F., Charbonneau, P. & López, G. P. Highly parallel acoustic
360 assembly of microparticles into well-ordered colloidal crystallites. *Soft Matter* **12**, 717–728 (2016).
- 361 15. He, M. *et al.* Colloidal diamond. *Nature* **585**, 524–529 (2020).
- 362 16. Shamloo, A. & Boodaghi, M. Design and simulation of a microfluidic device for acoustic cell
363 separation. *Ultrasonics* **84**, 234–243 (2018).
- 364 17. Simon, G. *et al.* Particle separation by phase modulated surface acoustic waves. *Biomicrofluidics* **11**,
365 (2017).
- 366 18. Ding, X. *et al.* Cell separation using tilted-angle standing surface acoustic waves. *Proceedings of the*
367 *National Academy of Sciences* **111**, 12992–12997 (2014).
- 368 19. Wu, M. *et al.* Acoustofluidic separation of cells and particles. *Microsystems & Nanoengineering* **5**,
369 (2019).
- 370 20. Ding, X. *et al.* On-chip manipulation of single microparticles, cells, and organisms using surface
371 acoustic waves. *Proceedings of the National Academy of Sciences* **109**, 11105–11109 (2012).

- 372 21. Supponen, O. *et al.* The effect of size range on ultrasound-induced translations in microbubble
373 populations. *The Journal of the Acoustical Society of America* **147**, 3236–3247 (2020).
- 374 22. Raymond, S. J. *et al.* A deep learning approach for designed diffraction-based acoustic patterning in
375 microchannels. *Scientific Reports* **10**, (2020).
- 376 23. Collino, R. R. *et al.* Acoustic field controlled patterning and assembly of anisotropic particles.
377 *Extreme Mechanics Letters* **5**, 37–46 (2015).
- 378 24. Pandey, H. D. & Leitner, D. M. Thermalization and Thermal Transport in Molecules. *The Journal of*
379 *Physical Chemistry Letters* **7**, 5062–5067 (2016).
- 380 25. Gorkov, L. P. On the Forces Acting on a Small Particle in an Acoustical field in an Ideal fluid. *Soviet*
381 *Physics Doklady* **6**, 773–775 (1962).
- 382 26. Bruus, H. Acoustofluidics 7: The acoustic radiation force on small particles. *Lab on a Chip* **12**, 1014
383 (2012).
- 384 27. Simon, Andrade, Desmulliez, Riehle, & Bernassau. Numerical Determination of the Secondary
385 Acoustic Radiation Force on a Small Sphere in a Plane Standing Wave Field. *Micromachines* **10**, 431
386 (2019).
- 387 28. Silva, G. T. & Bruus, H. Acoustic interaction forces between small particles in an ideal fluid. *Physical*
388 *Review E* **90**, (2014).
- 389 29. Barnkob, R., Augustsson, P., Laurell, T. & Bruus, H. Acoustic radiation- and streaming-induced
390 microparticle velocities determined by microparticle image velocimetry in an ultrasound symmetry
391 plane. *Physical Review E* **86**, (2012).
- 392 30. Crum, L. A. Bjerknes forces on bubbles in a stationary sound field. *The Journal of the Acoustical*
393 *Society of America* **57**, 1363–1370 (1975).
- 394 31. Shi, J. *et al.* Acoustic tweezers: patterning cells and microparticles using standing surface acoustic
395 waves (SSAW). *Lab on a Chip* **9**, 2890 (2009).

- 396 32. Collins, D. J. *et al.* Two-dimensional single-cell patterning with one cell per well driven by surface
397 acoustic waves. *Nature Communications* **6**, (2015).
- 398 33. Vakarelski, I. U., Li, E. Q., Abdel-Fattah, A. I. & Thoroddsen, S. T. Acoustic separation of oil droplets,
399 colloidal particles and their mixtures in a microfluidic cell. *Colloids and Surfaces A: Physicochemical
400 and Engineering Aspects* **506**, 138–147 (2016).
- 401 34. Garbin, A. *et al.* Acoustophoresis of disk-shaped microparticles: A numerical and experimental study
402 of acoustic radiation forces and torques. *The Journal of the Acoustical Society of America* **138**, 2759–
403 2769 (2015).
- 404 35. Glynne-Jones, P., Mishra, P. P., Boltryk, R. J. & Hill, M. Efficient finite element modeling of radiation
405 forces on elastic particles of arbitrary size and geometry. *The Journal of the Acoustical Society of
406 America* **133**, 1885–1893 (2013).
- 407 36. Tran, S. B. Q., Marmottant, P. & Thibault, P. Fast acoustic tweezers for the two-dimensional
408 manipulation of individual particles in microfluidic channels. *Appl. Phys. Lett.* **101**, 114103 (2012).
- 409 37. Nama, N. *et al.* Numerical study of acoustophoretic motion of particles in a PDMS microchannel
410 driven by surface acoustic waves. *Lab on a Chip* **15**, 2700–2709 (2015).
- 411 38. Devendran, C., Albrecht, T., Brenker, J., Alan, T. & Neild, A. The importance of travelling wave
412 components in standing surface acoustic wave (SSAW) systems. *Lab on a Chip* **16**, 3756–3766
413 (2016).
- 414 39. Barnkob, R. *et al.* Acoustically Driven Fluid and Particle Motion in Confined and Leaky Systems.
415 *Physical Review Applied* **9**, (2018).
- 416 40. Lord Rayleigh, F. R. S. XXI. On an Instrument capable of Measuring the Intensity of Aerial Vibrations.
417 *London, Edinburgh, Dublin Philosophical Magazine and Journal of Science* **14**, 186–187 (1882).
- 418 41. König, W. Hydrodynamisch-akustische Untersuchungen. *Annalen der Physik* **279**, 43–60 (1891).

419 42. Leng, Y. *Materials Characterization: Introduction to Microscopic and Spectroscopic Methods*. (Wiley-
420 VCH Verlag GmbH & Co. KGaA, 2008). doi:10.1002/9783527670772.

421 43. Trantidou, T., Elani, Y., Parsons, E. & Ces, O. Hydrophilic surface modification of PDMS for droplet
422 microfluidics using a simple, quick, and robust method via PVA deposition. *Microsystems &*
423 *Nanoengineering* **3**, (2017).

424

425 **Acknowledgements**

426 The authors acknowledge funding support from the CU Boulder startup fund and W. M. Keck Foundation
427 grant to X.D., and NIH grants R01CA195051 and R01HL151151 to M.B. G.S. acknowledges support
428 from Thomas and Brenda Geers Fellowship. A.K.F acknowledges support from the Teets Family
429 Endowed Doctoral Fellowship. The Microfluidic devices were fabricated in JILA clean room at
430 University of Colorado Boulder.

431 **Author Contributions**

432 G.S., T.Y, M.A.B. and X.D. designed the experiments; X.D. conceived the research; M.A.B. and X.D.
433 supervised the research; G.S. performed the experiments; T.Y. performed the simulations, Y.G. and
434 A.K.F. fabricated the devices. G.S. and T.Y. analyzed data. G.S., T.Y, Y.G., A.K.F., B.L. M.R., M.A.B.
435 and X.D wrote the paper.

436 # Equal contribution authors

437

438 **Competing Interests:**

439 The authors declare no competing interests.

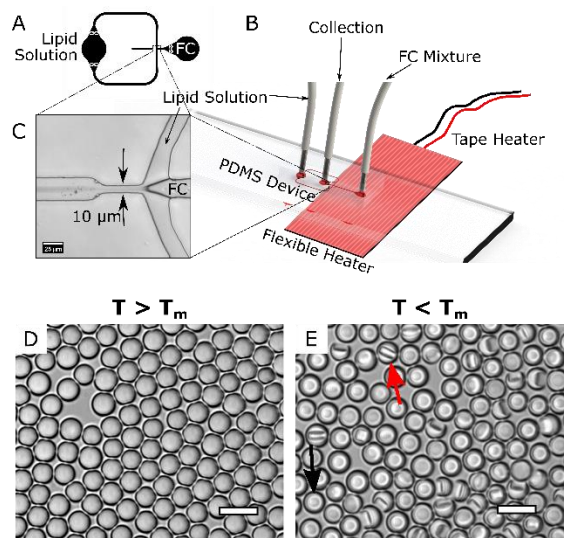
440 **Data availability**

441 All data needed to evaluate the conclusions in the paper are present in the paper and/or the Supplementary

442 Materials. Additional data related to this paper may be requested from the authors.

443

444

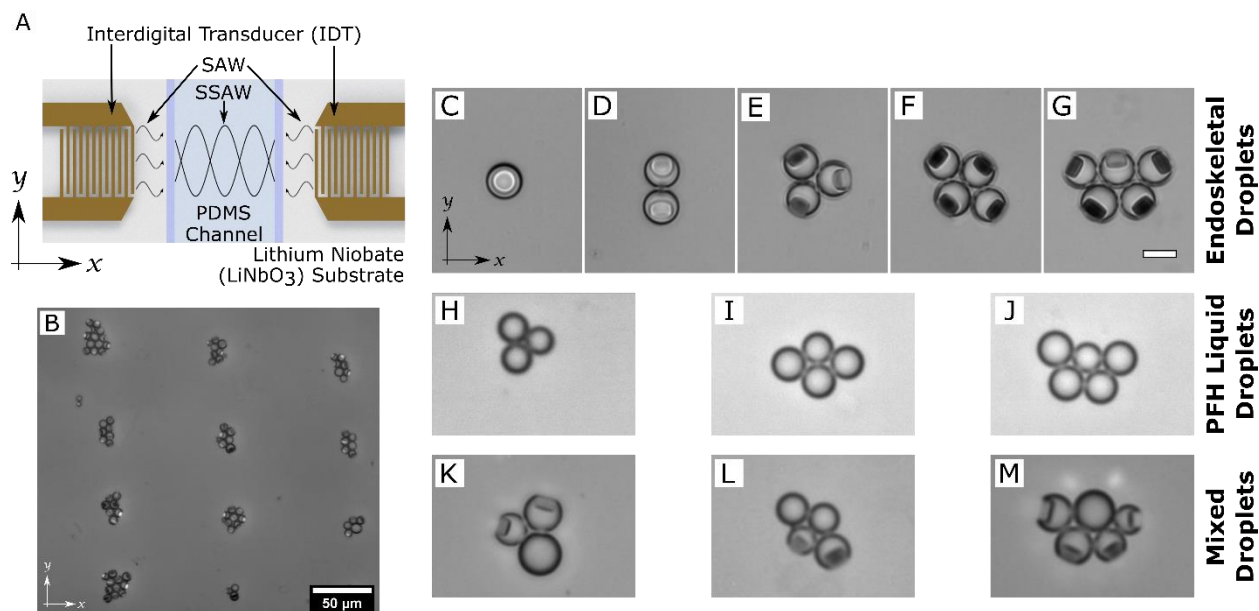


445 Figures

446

447 **Fig. 1. Microfluidic Fabrication of Endoskeletal Droplets.** **A.** Design of the Microfluidic Channel used to
 448 generate droplets. **B.** Droplet generation schematic showing the PDMS device and different inlets and outlets.
 449 Zoomed in image of the flow focusing junction is shown in **C.** Scale bar, 25 µm. **D.** Endoskeletal droplets generated
 450 using this technique at a higher temperature ($T > T_m$) are single-phase liquid droplets where the solid disks are all
 451 melted. When the droplets are cooled to a lower temperature ($T < T_m$), the solid phase separates and forms the
 452 endoskeleton confined by the droplet boundaries (shown in **E**). The disks are randomly oriented with different
 453 orientations. Parallel orientation of disk is shown by black arrow and perpendicular orientation of the disk is shown
 454 by red arrow. Scale bar, 20 µm.

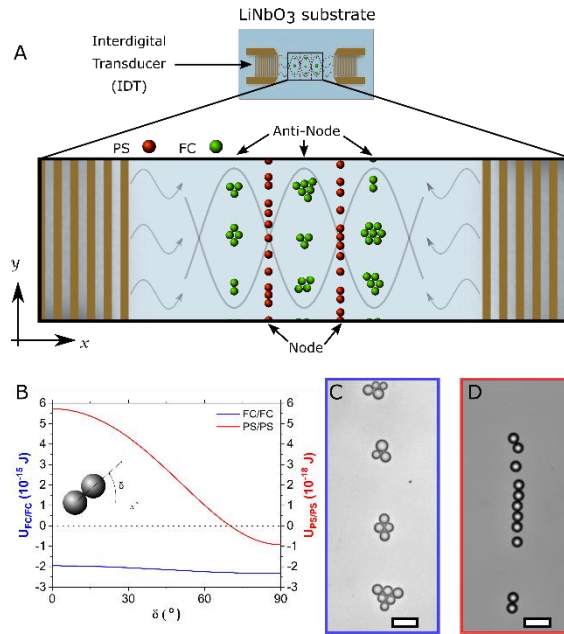
455



456

457 **Fig. 2. Endoskeletal Droplet Patterning under standing SAW.** **A.** Schematic of the SAW IDT devices used for
 458 patterning experiments. **B.** Clustering behavior of endoskeletal droplets under 1D standing SAW. Scale bar, 50 μm .
 459 Zoomed in images of the droplet clusters under 1D standing Saw with 1 droplet (**C**), 2 droplets (**D**), 3 droplets (**E**), 4
 460 droplets (**F**), 5 droplets (**G**). Note that the disk orientations are different for smaller clusters (**C** and **D**) compared to
 461 larger clusters (**E-H**). **H, I, J.** Liquid PFH droplet show similar clustering behavior as endoskeletal droplets. **K, L,**
 462 **M.** Clusters containing mixture of liquid only PFH droplets and endoskeletal droplets. Note that the clustering
 463 phenomenon is the same for all three types of droplets clusters and the disk orientations are not affected by the
 464 absence of other disks as well. Scale bar for all individual cluster images, 10 μm .

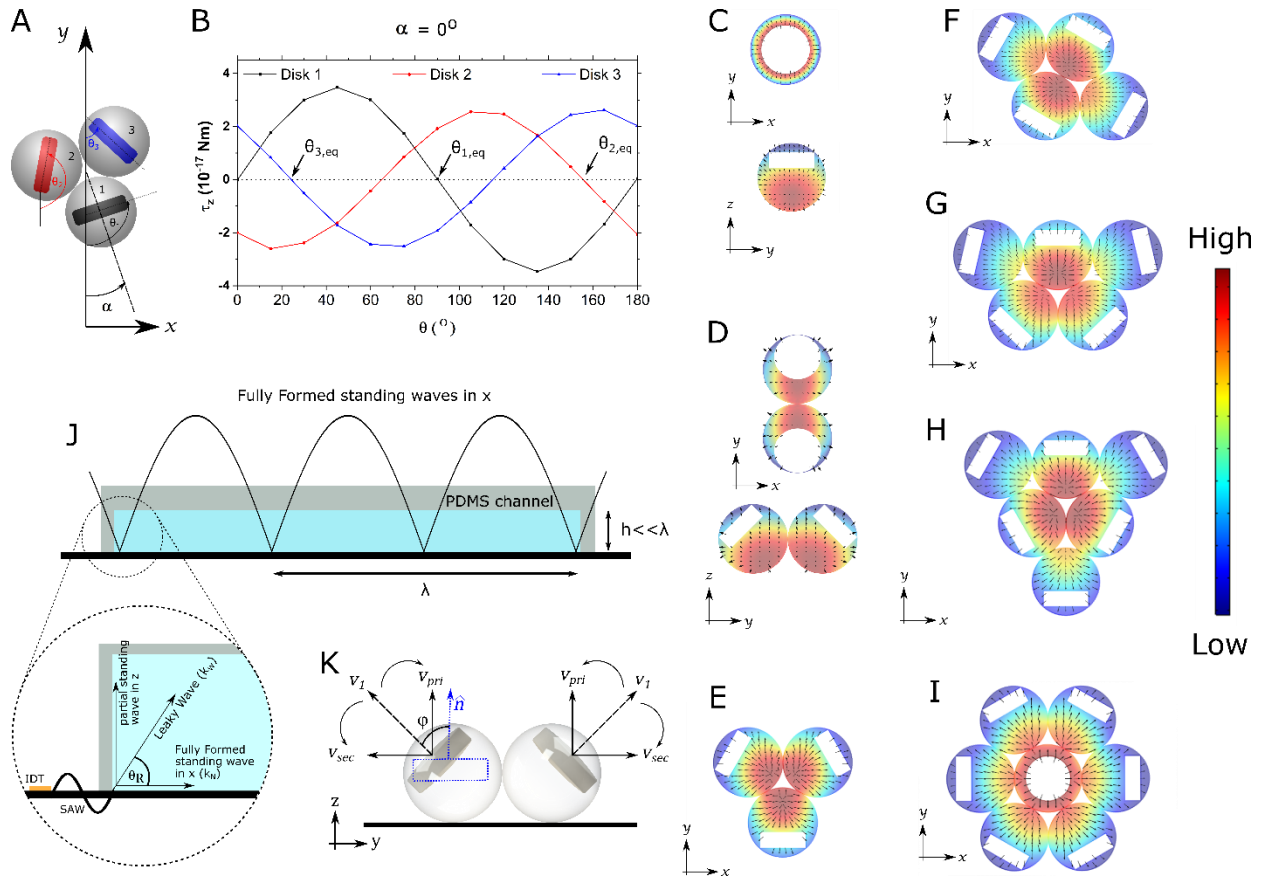
465



466

467 **Fig. 3. Liquid PFH droplet clustering and radiation forces.** A. Schematic of the SAW device shown with the
 468 assembly type and location of liquid PFH droplets and the PS beads of similar sizes. B. Secondary interaction
 469 energy between two contacting PFH droplets (red line, Eq. 4) and PS beads (blue line, Eq. S3) with orientation angle
 470 δ with respect to wave propagation direction, i.e., x-axis. Positive values indicate repulsion and negative values
 471 indicate attraction. C. Assembly of liquid PFH droplets under 1D standing SAW compared to the assembly of PS
 472 particles under 1D standing SAW (shown in D). Note that PS particles form chains whereas PFH particles forms
 473 clusters as shown by B. Scale bar, 20 μm .

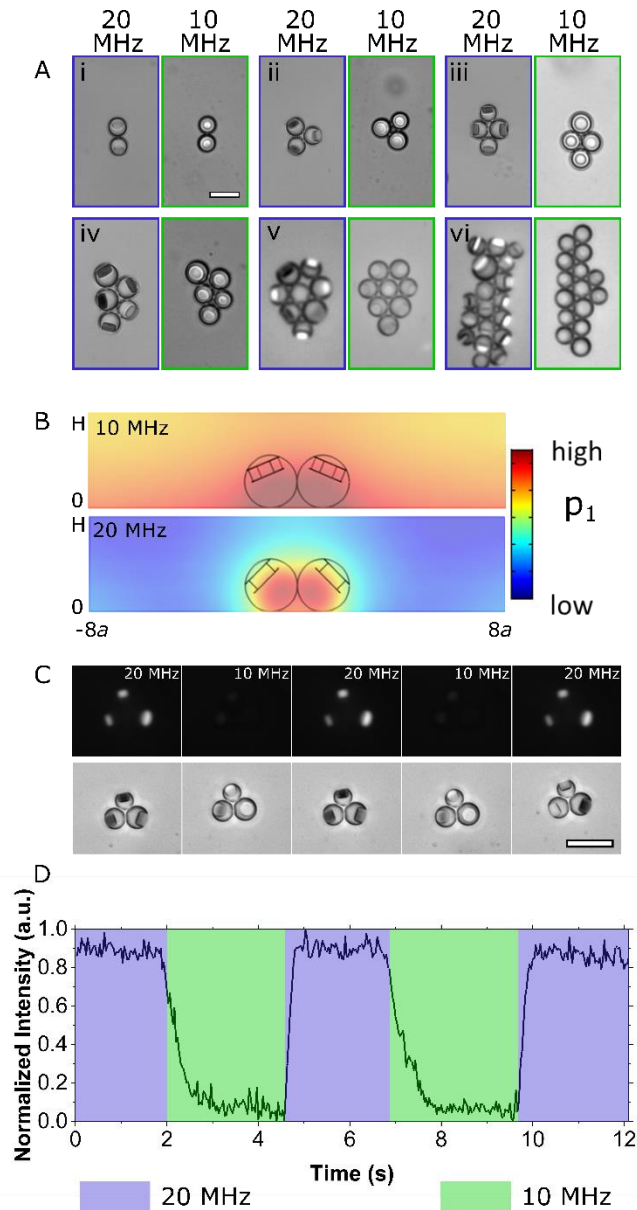
474



475

476 **Fig. 4. Understanding disk orientation behavior.** **A.** Schematic of disk orientation angles inside a trimer system
 477 plotted in **B.** **B.** Torque τ_z on inner disks inside a trimer cluster vs. disk orientation angle from COMSOL
 478 simulations. The equilibrium angles θ_{eq} (shown by arrows), i.e., equilibrium orientations are determined by the zero
 479 torques with negative slope. **C.** Simulation results showing the effect of standing SAW on clusters with 1 droplet
 480 (**C**), 2 droplets (**D**), 3 droplets (**E**), 4 droplets (**F**), 5 droplets (**G**), 6 droplets (**H**) and 7 droplets (**I**). The simulation
 481 results match the experimental observations of the droplet clusters shown in Fig. 2C-H, Supplementary Fig. 2. **J.**
 482 Schematic showing the generation of fully formed standing wave in the x-direction and partial standing wave in the
 483 z direction (due to restricted channel height). **K.** Schematic showing the disk orientation inside the droplet is a result
 484 of interplay between the primary and secondary radiation forces. φ is the angle between v_1 and the disk axis (shown
 485 in dotted blue for one of the droplets, with a random orientation, in a non-equilibrium position). At equilibrium
 486 torque, the disk radial symmetric axes should align with particle velocity v_1 direction ($\varphi = 0$), which is a sum of
 487 contributions from primary radiation v_{pri} (Along z-axis for all disks) and the secondary radiations v_{sec} (along radial
 488 direction away from the droplet cluster, i.e., y-axis for a 2 droplet cluster).

489



490

491 **Fig. 5. Effect of acoustic frequencies on the disk orientations.** A. clusters of endoskeletal droplets with 2 (i), 3
 492 (ii), 4 (iii), 5 (iv), 7 (v) and multiple (vi) droplets in the cluster at 20 MHz standing acoustic wave (left) and 10 MHz
 493 (right). Note that the solid disks are oriented parallel to the surface for 10 MHz whereas they are oriented
 494 perpendicular to the surface at 20 MHz. Scale bar, 20 μ m. B. Simulation results of dimer clusters in 10 MHz wave
 495 (top) and 20 MHz wave (bottom) showing total pressure distribution in the yz plane. The colors (red/blue) represent
 496 pressure amplitudes (high/low). Note that the pressure distribution between the two droplets (due to secondary
 497 radiation force) is more dramatic for 20 MHz than 10 MHz which results in a larger tilting angle for the solid disks
 498 at 20 MHz. C. Cross-polarized microscopy (top) images of a 3-droplet cluster where the disks are bright when they
 499 are perpendicular to the surface (20 MHz). Brightfield image of the same droplet cluster (bottom) shows the disk
 500 flipping between parallel and perpendicular just by changing input frequencies in a chirped IDT device (see
 501 Supplementary Movie 9 and 10). Larger droplet clusters are shown in Supplementary Fig. 10 and Supplementary
 502 Movie 11. Scale bar, 20 μ m. D. Plot corresponding to the normalized intensity from the cross polarized microscopy
 503 images recorded (C) while continuously changing frequencies every \sim 2.5 seconds. Purple area denotes 20 MHz
 504 whereas green area denotes 10 MHz.